

PAPER • OPEN ACCESS

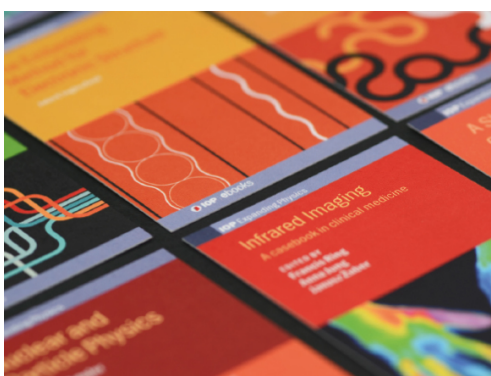
## High-performance dielectric nano-cavities for near- and mid-infrared frequency applications

To cite this article: Thanh Xuan Hoang *et al* 2022 *J. Opt.* **24** 094006

View the [article online](#) for updates and enhancements.

You may also like

- [Local Fisher- and skew-information coherence of two Nitrogen-Vacancy centers induced by two coupled dissipative nanocavities](#)  
A-B A Mohamed and Abdel-Haleem Abdel-Aty
- [Plasmonic structure with nanocavity cavities for SERS detection of pesticide thiram](#)  
Yongjun Zhang, Aonan Zhu, Yaxin Wang et al.
- [Surface plasmon polariton nanocavity with ultrasmall mode volume](#)  
Wencheng Yue, Peijun Yao, Huiwen Luo et al.



**IOP | ebooks™**

Bringing together innovative digital publishing with leading authors from the global scientific community.

Start exploring the collection—download the first chapter of every title for free.

# High-performance dielectric nano-cavities for near- and mid-infrared frequency applications

Thanh Xuan Hoang<sup>1,\*</sup> , Hong-Son Chu<sup>1</sup>, Francisco J García-Vidal<sup>1,2</sup> and Ching Eng Png<sup>1</sup>

<sup>1</sup> Department of Electronics and Photonics, Institute of High Performance Computing A\*STAR (Agency for Science, Technology and Research), 1 Fusionopolis Way, #16-16 Connexis, Singapore 138632, Singapore

<sup>2</sup> Departamento de Física Teórica de la Materia Condensada and Condensed Matter Physics Center (IFIMAC), Universidad Autónoma de Madrid, E-28049 Madrid, Spain

E-mail: [hoangtx@ihpc.a-star.edu.sg](mailto:hoangtx@ihpc.a-star.edu.sg)

Received 16 May 2022, revised 18 July 2022

Accepted for publication 3 August 2022

Published 17 August 2022



## Abstract

We present a judicious design approach for optimizing semiconductor nanocavities, starting from single photonic atoms to build photonic molecules functioning as high-performance nanocavities. This design approach is based on exact analytical solutions to the Maxwell equations for collective Mie resonances. Conceptually, we distinguish different concepts of cavity modes including Mie mode, collective Mie mode, photonic-crystal (PC) band-edge mode, and Feshbach-type bound states in the continuum (BIC) mode. Using the design approach, we present a unique structure of nanocavity supporting the Feshbach-type BIC mode, capable of enhancing the emission rate of a dipolar emitter by orders of magnitude. This high-performance nanocavity suppresses radiative loss channels strongly via destructive interference and consequently channels the emission light efficiently into an in-plane bi-directional beam with a divergence angle of  $10^\circ$ . Engineering the geometrical parameters of the nanocavity for near-infrared frequency applications requires a fabrication tolerance of  $\pm 5$  nm. This high accuracy is challenging for the mass production of devices. The fabrication accuracy can be relaxed greatly for mid-infrared frequency devices. As a showcase, we analyze and optimize the well-known PC L3 defect nanocavity for mid-infrared frequency applications in the framework of Feshbach resonance. We show that the optimal structure of this defect nanocavity requires a fabrication tolerance of  $\pm 50$  nm. Our nanocavity design approach may be useful for near- and mid-infrared frequency applications.

**Keywords:** nano-cavities, nanoantennas, collective resonance, Feshbach resonance, purcell factor, near-and mid-infrared frequency applications, bound states in the continuum (BIC)

(Some figures may appear in colour only in the online journal)

\* Author to whom any correspondence should be addressed.



Original content from this work may be used under the terms of the [Creative Commons Attribution 4.0 licence](https://creativecommons.org/licenses/by/4.0/). Any further distribution of this work must maintain attribution to the author(s) and the title of the work, journal citation and DOI.

## 1. Introduction

High-performance nanocavities are useful for a wide range of technological applications [1, 2] and fundamental science [3, 4]. Modern fabrication nanotechnology allows us to miniaturize photonic cavities to nanoscale in all three dimensions. Hence these photonic cavities can be engineered to have any given resonant mode and are also referred to as photonic atoms [5]. Even the lowest-order Mie modes of magnetic and electric dipoles have been demonstrated with semiconductor nanostructures functioning as photonic atoms [6]. Optically coupling these photonic atoms has resulted in a few interesting device structures such as Huygens metasurfaces [7] and strongly resonant nanochains [2]. Generally, these optically coupled atoms are known as photonic molecules [5]. A vast number of photonic molecules has been realized from the large degrees of freedom for design, offered by the number of atoms and their relative positions of geometrical arrangements [8, 9]. The photonic concepts associated with these photonic molecules usually originate from their counterparts in atomic, molecular, and condensed matter physics. Among those photonic concepts, bound states in the continuum (BICs) have recently received much attention due to their potential applications in quantum optics and functional optics [9, 10]. There are few definitions of BICs [11] of which BICs due to overlapping resonances can be analyzed in the framework of Feshbach's unified theory of nuclear reactions [12, 13]. Historically, Feshbach's resonance theory originates in nuclear physics [12] and is subsequently linked to atomic physics by Fano [14] who reformulates and extends his earlier work on the asymmetric resonance line shape due to the interference of a discrete autoionized state (a resonance) and a continuum [15]. Hence, sometimes Feshbach resonances are also known as Fano-Feshbach resonances that are the essential tool for important scientific breakthroughs [16]. In fact, Fano conceives his original theory for interpreting the asymmetric line shape, known as Fano profile nowadays, that is spectrally broad [15]. On contrary, Feshbach resonance is well-known to be spectrally narrow [17]. Here, we are interested in the interference of more than one resonance that results in an interfering resonance having an extremely narrow spectrum, and hence we attribute the physics to Feshbach's theory of overlapping resonances. At the heart of designing photonic molecules supporting these Feshbach-type BICs are geometrical parameters for tuning the frequencies of the constituent resonant modes continuously to achieve the optimal spectral overlap. Our previous work shows that spatial gaps between coupled photonic atoms play the role of the continuous parameters for optimizing the nanochain-based cavity [2]. However, Feshbach-type BICs have not been achieved with the single nanochain. Here we show that coupling three of such nanochains results in a unique photonic molecule functioning as a high-performance Feshbach-type BIC nanocavity. Our first-principle design and analysis of photonic molecules are based on rigorous analytical modelling which reveals the rich physics of collective Mie resonances [2, 8].

Theoretically, we can analyze single Mie resonances supported by single spheres [18, 19] in the framework of

a multipole expansion of electromagnetic field [20, 21]. In multipole analysis, multipole expansion coefficients (MECs) are of importance in, for example, determining the resonant strengths of cavity modes [22] and analyzing tightly focused laser beams [23, 24]. For optically coupled spheres, analytical modelling can be formulated for calculating the relevant MECs [2, 8, 25]. This work emphasizes the usefulness and convenience of using MECs in designing Mie resonances and their response in unison. We discuss single Mie resonances supported by sphere and pillar in sub-section 2.1. Subsequently, we present collective Mie resonances supported by linear nanochains of the spheres and pillars in sub-section 2.2. Sub-section 2.3 presents Feshbach resonances resulting from the unique structure of three optically coupled nanochains. In section 3, we further use Feshbach theory of overlapping resonances for analyzing and optimizing the well-known L3 photonic-crystal (PC) defect cavity. We conclude the importance of our judicious design approach to high-performance nanocavities for near- and mid-infrared (mid-IR) photonic applications in section 4.

## 2. Lorenz–Mie theory and collective Mie resonances

Exact analytical solutions to the Maxwell equations are rare and Lorenz–Mie theory provides such solutions to the electromagnetic scattering of a plane wave by a homogeneous isotropic dielectric sphere. The simplicity of the scattering problem and its exact analytical solutions to the Maxwell equations make the Lorenz–Mie theory appears in almost all classical textbooks introducing optics and electromagnetism. We present the vast literature on the theory and its generalized version for shaped laser beams in our previous work [18]. We also document and implement exact solutions to the Maxwell equations for the electromagnetic scattering by clusters of spheres before [2, 8]. Here we summarize the main formulae for the convenience of discussion.

### 2.1. Single photonic atoms

Figures 1(a) and (b) show the simplest configurations for the interaction between an electric dipolar (ED) emitter and single photonic atoms represented by the sphere and pillar. In figure 1(a), the emitter is exterior to the photonic atom and may represent quantum emitters, such as semiconductor quantum dots or rare-earth ions. In figure 1(b), the emitter is inside the photonic atom and may represent defects in solids. Strictly speaking, quantum electrodynamics need to be invoked for calculating the interaction energy between the emitter and its environment [26, 27]. Nevertheless, in the weak coupling regime, the full quantum calculation agrees well with the classical analysis of the interaction energy [28, 29]. This work presents classical calculations and the ED emitter will be represented by a predetermined classical ED source. In addition, we assume materials of photonic structures to be dispersionless and lossless dielectric.

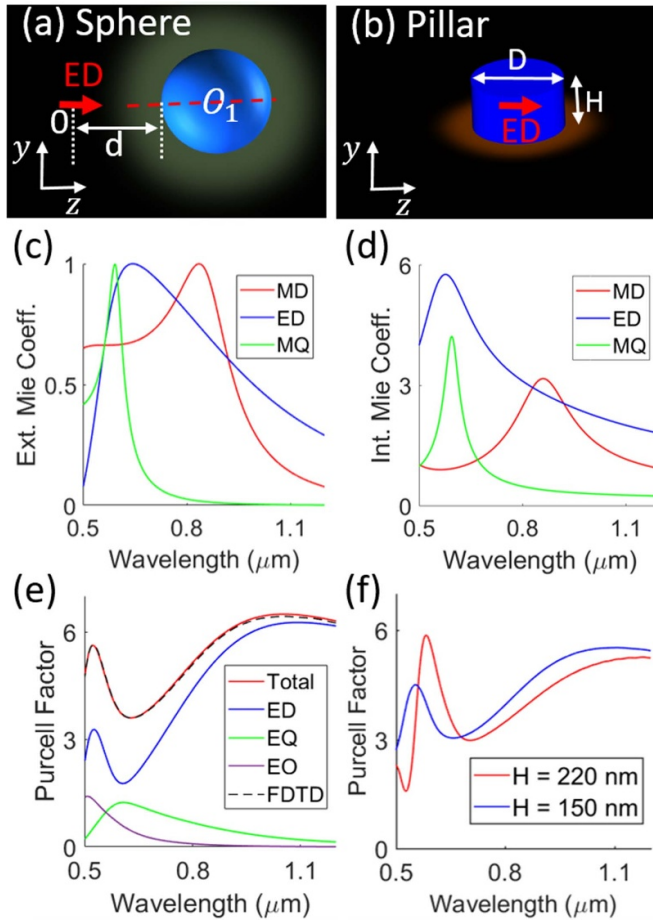


**Figure 1.** Interaction between an electric dipolar (ED) emitter and single photonic atoms. (a) Schematic of the ED emitter exterior to the sphere.  $O$  and  $O_1$  are the origins of the coordinate systems associated with the emitter and the sphere, respectively. (b) The emitter inside the pillar. (c) and (d) Spectral response of the external and internal magnetic dipole (MD), electric dipole (ED) and magnetic quadrupole (MQ) Mie coefficients. The contrast of the refractive indices between the sphere and its environment is 3.65/1.45. The sphere's radius is  $R = 110$  nm. (e) Spectral plot of the Purcell factor when the longitudinal ( $z$ -oriented) ED emitter situates 10 nm away from the sphere's surface, i.e.  $d = 10$  nm. We decompose the total Purcell factor into the contributions due to the coupling to the electric dipole (ED), quadrupole (EQ) and octupole (EO) field emission. The FDTD simulation agrees excellently with the multipole theory. (f) We replace the sphere in (e) with a pillar having the same radius, i.e.  $D = 220$  nm; and we simulate the Purcell factor with two different heights of the pillar:  $H = 220$  nm and  $H = 150$  nm.

**2.1.1. Multipole field theory for the interaction between a sphere and a multipolar emitter.** For the single sphere in figure 1(a), we can express the incident electric field in terms of regular electric  $N_l^m$  and magnetic  $M_l^m$  eigenfunction multipole fields as follows [2, 8]:

$$\mathbf{E}^{\text{inc}}(\mathbf{r}_1) = \sum_{l=1}^{L_{\text{max}}} \sum_{m=-l}^l [p_{lm} \mathbf{N}_l^m(k\mathbf{r}_1) + q_{lm} \mathbf{M}_l^m(k\mathbf{r}_1)] \quad (1)$$

where  $\mathbf{r}_1$  is the field's position in the  $O_1$ -coordinate system;  $k$  is the wave-number of the field's associated wave;  $p_{lm}$  and  $q_{lm}$

are the electric and magnetic MECs, respectively. Equation (1) can represent the electric field radiated by an arbitrary well-behaved, localized, monochromatic multipolar emitter [20]. For an ED emitter, the dipole field in its own  $O$ -coordinate system is translationally equivalent to many different eigenfunction multipole fields approaching the spherical photonic atom. In other words, the MECs representing the same radiating field are different in different coordinate systems. The truncated number  $L_{\text{max}}$  depends on the distance between the two coordinate origins  $O$  and  $O_1$ . In the Lorenz–Mie theory, the scattering  $\mathbf{E}^{\text{sct}}$  and internal  $\mathbf{E}^{\text{int}}$  fields are

$$\mathbf{E}^{\text{sct}}(\mathbf{r}_1) = \sum_{l=1}^L \sum_{m=-l}^l [a_l p_{lm} \mathbf{N}_{lm}(k\mathbf{r}_1) + b_l q_{lm} \mathbf{M}_{lm}(k\mathbf{r}_1)] \quad (2)$$

$$\mathbf{E}^{\text{int}}(\mathbf{r}_1) = \sum_{l=1}^L \sum_{m=-l}^l [c_l p_{lm} \mathbf{N}_l^m(k_1\mathbf{r}_1) + d_l q_{lm} \mathbf{M}_l^m(k_1\mathbf{r}_1)], \quad (3)$$

where  $\mathbf{N}_{lm}$  and  $\mathbf{M}_{lm}$  are the outgoing electric and magnetic eigenfunction multipole fields [21], respectively;  $k_1$  is the wave-number of the wave corresponding to the internal field;  $a_l$  ( $c_l$ ) and  $b_l$  ( $d_l$ ) are the external (internal) electric and magnetic Mie scattering coefficients [2, 8, 18, 22], respectively. The highest multipole order  $L$  in equations (2) and (3) is the upper limit of  $L = kR + 4.05\sqrt[3]{kR} + 2$  where  $R$  is the radius of the sphere. In the literature, the regular and outgoing eigenfunction multipole fields are also known as partial multipole fields that are exact solutions to the Maxwell equations in the framework of the Lorenz–Mie theory. The appearance of the MECs  $p_{lm}$  and  $q_{lm}$  in all of the three equations (1)–(3) means that the dipolar emitter can excite all of the eigenfunction multipole fields of the sphere, depending on the dipole's orientation and its relative position to the sphere.

Spontaneous emission of an emitter is one of the most celebrated phenomena in quantum electrodynamics. The interest in the phenomenon is partly due to the fact that the rate of emission is not the emitter's intrinsic property but depends on its environment [30]. The key quantity for quantifying this environment dependence is the power radiating into the far-field region. In our case, the material is lossless, and consequently, the radiating power  $P$  equals the rate of energy dissipation from the dipolar emitter according to the following formula [29]

$$P = \frac{\omega}{2} \text{Im} \{ \bar{\boldsymbol{\mu}}^* \cdot \mathbf{E}(\mathbf{r}_\mu) \} \quad (4)$$

where  $\bar{\boldsymbol{\mu}}^*$  and  $\omega$  are the conjugate electric dipole moment and angular frequency associated with the dipolar transition;  $\mathbf{E}(\mathbf{r}_\mu)$  is the local electric field acting on the dipole. For the predetermined classical dipole source, we can set  $\bar{\boldsymbol{\mu}}^* = 1$  without loss of generality; additionally, instead of considering the absolute value of the spontaneous emission rate associated with a specific emitter, we will study the environment dependence in terms of the Purcell factor as defined by [2, 29, 30]

$$F_P = \frac{P}{P_0} \quad (5)$$

where  $P_0$  is the power radiated by the dipole in the corresponding homogeneous material. Equations (4) and (5) form the near-field approach to estimating the Purcell factor.

Alternative to the near-field approach, we can estimate the Purcell factor in terms of the total far field comprising the field directly radiated by the emitter, which in the  $O_1$ -coordinate system is denoted as the incident field  $\mathbf{E}^{\text{inc}}$ , and the scattered field  $\mathbf{E}^{\text{sct}}$ :

$$\mathbf{E}^{\text{tot}}(\mathbf{r}_1) = \mathbf{E}^{\text{inc}}(\mathbf{r}_1) + \mathbf{E}^{\text{sct}}(\mathbf{r}_1) = \sum_{l=1}^{L_{\text{tot}}} \sum_{m=-l}^l [\alpha_{lm} \mathbf{N}_{lm}(k\mathbf{r}_1) + \beta_{lm} \mathbf{M}_{lm}(k\mathbf{r}_1)]. \quad (6)$$

An important note for equation (6) is that we need to expand the field  $\mathbf{E}^{\text{inc}}$  in terms of the outgoing eigenfunction multipole fields instead of the regular counterparts as in equation (1). This difference comes from applying the translational addition theorem for expressing the electromagnetic field in the different spatial regions [2, 8, 22, 24]. Another important note is about the truncated number  $L_{\text{tot}}$  that depends on the size of the whole system including the emitter and the photonic structure. Generally, we need more multipole eigenfunctions with higher orders to describe the total field radiating from larger systems. After evaluating the MECs  $\alpha_{lm}$  and  $\beta_{lm}$ , we can compute the power radiating into the far-field region as follows [20]:

$$P = \frac{c}{8\pi} \sum_{l=1}^{L_{\text{tot}}} \sum_{m=-l}^l l(l+1) [|\alpha_{lm}|^2 + |\beta_{lm}|^2]. \quad (7)$$

Equations (5) and (7) form the far-field approach to the estimation of the Purcell factor.

Now, we are ready to analyse different photonic concepts by using the above analytical formulae for a near-IR frequency ED emitter. Particularly, we are interested in the emission wavelength of 830 nm that is commercially relevant to the technology of optical interconnect [2]. For this wavelength we use the refractive indices of 3.65 (gallium arsenide) and 1.45 (glass) for the materials of the photonic atoms and their environment, respectively. Figures 1(c) and (d) show the spectral plots of the magnitudes of the three lowest-order Mie coefficients for the sphere with a radius of 110 nm. This specific radius ensures the peak resonance of the magnetic dipole occurring at the near-IR wavelength. Notably, unlike the whispering-gallery high-order Mie modes having the same Lorentzian spectral profiles [8], the spectral shapes of the external and internal low-order Mie coefficients in figures 1(c) and (d) are different. These spectral differences have profound implications for the near- and far-field analyses of the emitter-sphere interaction. For instance, figure 1(e) shows the spectral plot of the Purcell factor associated with the longitudinal ED emitter pointing through the centre of the sphere. For this interaction configuration, the emitter couples with only the electric multipole fields [2, 8] and in the spectral range from 0.5  $\mu\text{m}$  to 1.1  $\mu\text{m}$ , only the electric dipole eigenmode is on resonance with its peak wavelength of 0.578  $\mu\text{m}$  as shown in figure 1(d). However, this peak wavelength is near the trough between the two peaks of the Purcell factor. In other words, the radiating

power is near minimum when the internal near field is maximum. This counterintuitive observation is due to the interference between the directly radiating field from the emitter and the indirect radiation from the sphere via the Mie scattering. The external Mie coefficients account only for the indirect radiation and hence we cannot infer the spectral plot of the Purcell factor solely from the Mie coefficients. To understand the spectral plot further, we decompose the Purcell factor into components due to the different partial multipole fields as expressed in equation (7). At the longer wavelength, the energy approaches the far-field region mainly in the form of a dipole wave but at the shorter wavelength, the contributions of the other partial multipole fields become significant. Generally, the weights of these contributions depend on the relative position between the emitter and the sphere, which governs the interference of the partial multipole fields. This interference enables us to engineer the far-field radiation pattern as shown in the later section about collective resonances.

Another interesting topic relating to the interpretation of the Mie coefficients is the physics of nonradiating anapole modes [31]. Figures 1(c) and (d) show that near the wavelength of 0.5  $\mu\text{m}$  the external ED coefficient approaches zero, meanwhile the corresponding internal ED coefficient is larger than 3, indicating that the sphere can store energy under the form of the dipole displacement current. In the generalized Lorenz–Mie theory, we show in our previous work [23] that under a complete  $4\pi$  focusing, the radially polarized beam can mimic a converging dipole field perfectly. Using this dipole-mimicked beam with the appropriate wavelength near 0.5  $\mu\text{m}$  to excite the sphere would result in no scattering field and simultaneously there is a field enhancement inside the sphere [32]. Experimental demonstration with a partial illumination beam has verified both of these far- and near-field phenomena. Due to the imperfect illumination, the experimental demonstration results in a minimum in the spectrum of the scattering light intensity and the corresponding enhancement in the near-field distribution [31]. One may associate, mistakenly, with this dipole current as one example of nonradiating classical current distributions [33]. This attribution is indeed inappropriate when we consider the dynamics of the field. The Lorenz–Mie theory (Mie coefficients) is known to be valid for studying the stationary scattering effects only since the Mie coefficients include the retardation effects implicitly; and one has to invoke Debye series for analysing the dynamics of the scattering field [18, 24]. With the Debye series, one can show easily that after we turn off the excitation beam, the internal field of the sphere gradually reduces to zero, i.e. the energy stored in the dipole displacement current will leak into the far-field region. On contrary, the near-field distributions of nonradiating classical current distributions will not vanish while their external field must vanish in accordance [33] with equation (7). In fact, without a localized source and within the framework of classical Maxwell equations, for dielectric systems with real refractive indices and finite volumes, there is no bound modes [34], i.e. there are no anapole modes resulting from displacement-current distributions.

Figure 1(e) also presents the accuracy and advantage of our multipole theory. Our estimation of the Purcell factor agrees

excellently with that based on the near-field approach estimated by an finite-difference time-domain (FDTD) commercial software [35]. To achieve the excellent agreement, we need to perform the FDTD numerical simulation with a fine mesh size of 2.5 nm for the sphere placed at the centre of a simulation box having a volume of  $1.4 \times 1.4 \times 1.4 \mu\text{m}^3$ . This fine mesh size makes the numerical simulation inefficient in time in comparison with our analytical formulae.

**2.1.2. Mie resonances with pillar photonic atoms.** Photonic atoms with spherical shapes are challenging for fabrication. In this regard, pillars with cylindrical shapes have been widely used for lasing applications and flat optics. Figure 1(f) shows that using a pillar we can obtain the spectrum of the Purcell factor similar to that of the sphere presented in figure 1(e). For the first spectral plot, we use the pillar with the height and diameter equal to the diameter of the sphere, i.e.  $H = 220$  nm and  $D = 220$  nm. In comparison with the sphere, the pillar offers one more degree of freedom for cavity design; the vertical  $y$ - and horizontal  $z$ -dipole modes supported by the pillar are generally different (see figure 1(b) for schematic). With this degeneracy lifting, there is another trough appearing on the red spectrum in figure 1(f) and relative to the sphere's spectrum, the pillar's spectrum shifts to the longer-wavelength side. Reducing the height from 220 nm to  $H = 150$  nm moves the resonance of the  $y$ -dipole mode to the shorter-wavelength side and hence we obtain the spectral shape similar to that of the sphere.

Before we proceed to discuss collective resonances supported by photonic atoms arranged judiciously to form photonic molecules functioning as high-performance nanocavities, we present useful relations between the electric (magnetic) fields at the centre of the photonic atoms and their ED (MD) expansion coefficients. When the emitter is exterior to the photonic atoms, regardless of their shape we may expand the internal field as follows:

$$\mathbf{E}^{\text{int}}(\mathbf{r}_1) = \sum_{l=1}^L \sum_{m=-l}^l [\zeta_{lm} \mathbf{N}_l^m(k_1 \mathbf{r}_1) + \eta_{lm} \mathbf{M}_l^m(k_1 \mathbf{r}_1)]. \quad (8)$$

At the centre of the photonic atom, only the ED and MD fields exist, i.e. all the eigenfunction multipole fields with  $l > 1$  do not contribute to the electromagnetic field at  $\mathbf{r}_1 = 0$ . The expressions of the regular dipole fields are simple that can be found in our previous publication [23]. We then convert the field components from the spherical coordinates to the Cartesian coordinates so that we can express the spherical dipolar coefficients in terms of the Cartesian components of the electromagnetic field. Consequently, equation (8) and their magnetic counterpart reduce to [2]

$$\zeta_{1;0} = \sqrt{\frac{3}{8\pi}} \lambda E_z, \quad \zeta_{1;\pm 1} = \frac{1}{2} \sqrt{\frac{3}{8\pi}} \lambda (E_x \mp iE_y), \quad (9)$$

$$\eta_{1;0} = \sqrt{\frac{3}{8\pi}} \lambda H_z, \quad \eta_{1;\pm 1} = \frac{1}{2} \sqrt{\frac{3}{8\pi}} \lambda (H_x \mp iH_y), \quad (10)$$

where  $\lambda$  is the wavelength in the corresponding material;  $E_x$ ,  $E_y$ , and  $E_z$  ( $H_x$ ,  $H_y$  and  $H_z$ ) are the Cartesian components of the electric (magnetic) field. The linear relations presented in equations (9) and (10) are useful for multipole analysis involving non-spherical photonic atoms.

## 2.2. Collective Mie resonances

Photonic atoms can store energy in the form of polarization of their material. The Maxwell equations govern evolution of the energy. We can write the equations of motion for light propagation in Schrödinger form and show that the light potential is always smaller than the light energy [34]. Consequently, there is no bound state for light in dielectric systems. Intriguingly, photonic BICs have recently gained significant attention, mainly due to the potential of their associated cavities in trapping light with infinite quality factor (Q factor) [11].

Theoretically, Q factors of collective Mie resonances could be infinite, given an infinite number of constituent photonic atoms [2]. In other words, we can design a cavity supporting infinitely narrow resonances with the condition that we can extend the cavity to infinity. Satisfying this condition of infinity is also a requirement for the original BIC to exist [36]. Historically, the BIC concept originates from the diffractive interference of a matter wave corresponding to a positive-energy eigenstate of an infinite potential structure. Nevertheless, positive-energy eigenstates of electromagnetic waves, also known as band-edge eigenstates of infinite periodic material structures, are known to exist even decades earlier than the original BIC [37]. Today, these band-edge eigenstates are useful in designing distributed feedback laser cavities. In fact, the collective Mie resonances with the infinite Q factors also correspond to the band-edge modes of the corresponding PC; these band-edge modes correspond to the Van Hove singularities of the local density of photonic states [2]. These singularities and their associated infinite Q factors make the optimization process theoretically unnecessary. However, structures extending to infinity are impractical.

For practically finite structures, no BIC or photonic Van Hove singularity could exist [11]. Despite this fact, the BIC concept is still useful, for example, in lasing applications [38, 39]. To distinguish these so-called BICs in the finite structures—and hence BICs with finite Q factors—with normal cavity modes, the dramatic increases of the Q factors near the optimal tuning parameters have been used to identify BIC-inspired cavities [40]. For the collective Mie resonances supported by a finite nanochain of 100 pillars, we show in [2] that the optimization of the inter-particle gaps results in the orders-of-magnitude enhancements of the Q and Purcell factors. Equally important, we show that all the nanochains with more than 50 pillars function effectively as PCs since the resonant wavelengths of the collective Mie resonances converge to the PC band-edge modes [2]. This sub-section will focus on a unique cavity structure of three coupled nanochains with each nanochain comprising 21 pillars. We will show that the unique arrangement of the photonic atoms results in a single-mode Feshbach-type BIC nanocavity. Coupling

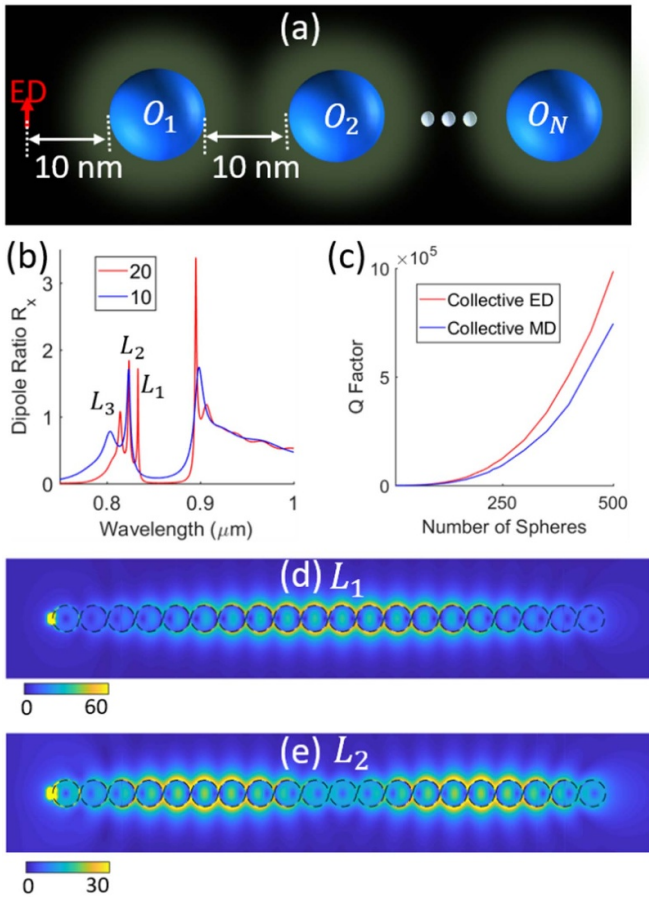


**Figure 2.** Collective Mie resonances with spheres. (a) Schematic of a transverse ED emitter interacting with the linear chain of  $N$  identical spheres. (b) The ratio of the electric dipole moments from the multipole field expansions of the internal fields of the first and last spheres of the two nanochains:  $N = 10$  and  $N = 20$ . (c) Divergence of the Q factors of the collective electric (ED) and magnetic (MD) dipole resonances with the increasing number  $N$ . (d) and (e) Electric field distributions of the two collective resonances marked in (b).

this nanocavity with an ED emitter results in a bidirectional nano-beam with the two main lobes diverging within two solid angles of less than  $10^\circ$ .

**2.2.1. Optically coupled spheres.** We presented rigorous mathematical modelling of collective Mie resonances supported by chains of spheres, such as one in figure 2(a), in our previous works [2, 8]. Here we use the model for analyzing a nanochain of identical spheres having the same parameters with the sphere in figure 1. In addition, we will consider collective dipole modes excited by a transverse ED emitter since these modes correspond to the smallest physical footprint of nanocavities [2]. To reach the last sphere, the light emission from the emitter propagates through the whole nanochain and consequently, the internal field of the last sphere contains the signature of all of the collective Mie resonances that are trapped inside the nanochain. To detect all of the collective Mie resonances and their corresponding PC bands [2], we estimate the dipole ratio  $R_x$  between the dipole coefficients from

multipole field expansions of the internal fields of the first and last spheres of the nanochain. Figure 2(b) shows the results for two nanochains comprising 10 and 20 spheres, respectively. We can observe the collective Mie resonances embedded in the two spectral PC bands. We label these two bands as ED and MD bands since the ED (MD) field accounts mainly for the spheres' electric (magnetic) internal field for the band at the wavelength of  $0.83 \mu\text{m}$  ( $0.9 \mu\text{m}$ ). The 20-sphere nanochain supports three collective ED resonances marked by  $L_1, L_2$  and  $L_3$ . The narrowest resonance is the  $L_1$  mode in which the electric field localizes mainly at the centre of the nanochain as shown in figure 2(d). Here, it is noteworthy that we use the multipole expansion with the order up to  $L = 7$  (based on the formula  $L = kR + 4.05\sqrt{kR} + 2$ ) for describing the internal fields of the spheres in figure 2(d). Figure 2(e) shows the electric field distribution of the  $L_2$  mode that has a minimum at the centre. The  $L_2$  mode is similar to a combination of two  $L_1$  modes supported by the 10-sphere nanochains. The spectral coincidence between the 10-sphere  $L_1$  and the 20-sphere  $L_2$  modes in figure 2(b) corroborates the field observation. Figure 2(c) shows the effect of the number of spheres on the Q factor of the collective ED ( $L_1$  mode) and MD resonances. As expected, the Q factors of the band-edge modes diverge rapidly with the increasing number of spheres. But these factors are always finite for practically finite structures.

Spherical shape is convenient for mathematical modelling and mode analysis but it would be more challenging for fabrication than the cylindrical shape. Therefore, the rest of this section will focus on nanochains of pillars.

**2.2.2. Optically coupled pillars.** Figure 3(a) shows a schematic of a nanochain comprising 20 pillars. Topologically, pillar and sphere are the same, and sub-section 2.1 showed already that the pillar with the diameter  $D = 220 \text{ nm}$  and height  $H = 150 \text{ nm}$  and the sphere with the same diameter, when interacting with the ED emitter, result in a similar spectrum. Here, we use this pillar with a slightly smaller radius of  $212 \text{ nm}$  as photonic atoms to build the 20 pillar nanochain. The smaller radius ensures the resonant wavelength of the  $L_1$  mode to be around  $0.83 \mu\text{m}$ . Figure 3(b) shows the Purcell factor associated with the transverse ED emitter placed at the centre of the 10th sphere when the inter-particle gap is  $G = 5 \text{ nm}$ . Only the two modes  $L_1$  and  $L_3$  appear in figure 3(b). As we discussed in the subsection of 2.2.1, the field distribution of a collective  $L_2$  mode has a minimum at the centre of the nanochain; hence the transverse ED emitter in figure 3(a) does not couple with the  $L_2$  mode. Figures 3(c) and (d) present the imaginary component of the electric field  $E_x$  and the radiation pattern associated with the  $L_1$  mode, respectively. We can perceive the enhancement of the Purcell factor by comparing the imaginary components corresponding to different nanocavity structures since according to equation (4) the radiating power is proportional to the imaginary component of the electric field for the case of constant dipole moment. Figure 3(e) displays the radiation pattern in the transverse plane that reveals a  $40^\circ$  diverging solid angle of the bidirectional nano-beam produced by the emitter-nanochain interaction.

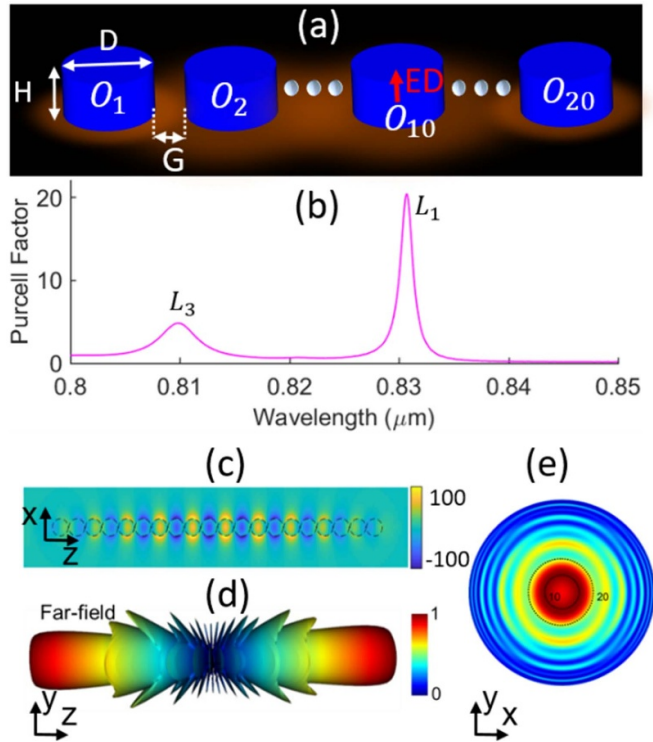


**Figure 3.** Collective resonances of the transverse EDs supported by the 20 identical pillars with  $H = 150$  nm and  $D = 212$  nm. The gap distance is  $G = 5$  nm. (a) Schematic of the nanochain. (b) Spectral plot of the Purcell factor associated with the transverse ED emitter placed at the centre of the 10th pillar. (c) The imaginary component of the near-field  $E_x$  distribution corresponding to the collective resonant mode  $L_1$  and (d) its corresponding far-field radiation pattern. (e) The radiation pattern plotted in the transverse plane shows the main lobe diverging into a solid angle of  $40^\circ$  (from  $-20^\circ$  to  $20^\circ$ ) at its full-width at half-maximum intensity.

The Purcell factor associated with the  $L_3$  mode is lower than that of the  $L_1$  mode, suggesting the dominance of the  $L_1$  near-field strength in accordance with equation (4). The field dominance of the  $L_1$  mode over the  $L_2$  mode may be appreciated from figures 2(d) and (e). More details about these modes can be found in our previous work [2]. The appearance of the two  $L_1$  and  $L_3$  modes in figure 3(b) inspires us to find a tuning parameter for designing a Feshbach-type BIC nanocavity based on the nanochain. We present the two simplest tuning approaches to tune the two modes in figure 4.

**2.2.3. Two spectral tuning approaches.** Figure 4(a) presents the schematic with the definitions of the two tuning parameters: the gap  $G = P - D$  with the nanochain's period  $P$  and the number of pillars  $N$ . A negative value of  $G$  corresponds to a spatial overlap between the adjacent pillars. For plots in figures 4(b) and (c), we use the diameter of the pillars to be  $D = 212$  nm and for this particular case, the effects of tuning the gap  $G$  and the period are the same. Generally, the inter-particle gap  $G$  plays the decisive role in the nanocavity performance since it determines the overlap between the fields trapped by the adjacent pillars. Meanwhile, the diameter  $D$  has a dominant role in determining the resonant

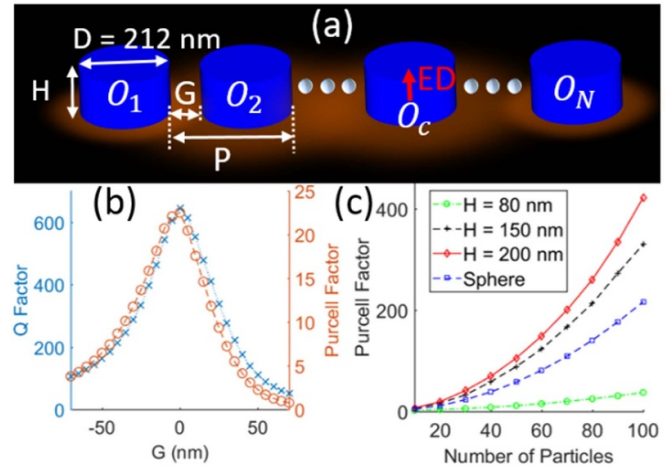


**Figure 4.** Nanocavity optimization with gap tuning and dependence on pillars' height of the divergence rate of the Purcell factor with an increasing number of photonic atoms  $N$ . (a) Schematic of the interaction between the  $N$ -pillar nanochain and the transverse ED emitter placed at the central pillar  $O_c$ . (b) Dependence of the Q and Purcell factors on the inter-particle gap  $G$  for the 20-pillar nanochain with  $H = 150$  nm. The negative value of  $G (=P - D)$  represents the spatial overlap between two adjacent pillars, i.e. the period  $P$  is less than the diameter  $D$ . (c) The Purcell factor diverges at different rates, depending on the height  $H$ . The result for the sphere nanochain is presented for comparison. The suboptimal gap of  $G = 10$  nm is used for all four plots.

wavelength. Therefore, our judicious design approach starts with a photonic atom and then continues with optimization of the geometrical arrangement of the identical photonic atoms. Figure 4(b) presents the optimization approach based on tuning the inter-particle gap of the 20-pillar nanochain. The gap dependence of Q and Purcell factors reveals the optimal gap of  $G = 0$  nm. Both the Q and Purcell factors do not change dramatically with the varying gap  $G$ . The gap range corresponding to the full width at half maximum (FWHM) of the factors is 50 nm. In addition, even with the optimal gap the two modes are still spectrally separated by 20 nm as one may appreciate from figure 3(b) for the near-optimal gap  $G = 5$  nm.

Alternatively, we can tune the two modes to be closer spectrally by increasing the number of particles. This tuning approach is conceivable from the fact that the resonant wavelengths the  $L_1$  and  $L_3$  modes associate with the collective resonances of the  $N$  and  $N/3$  particles, respectively; hence when  $N$  approaches infinity, both of the resonant wavelengths will converge to the resonant wavelength of the corresponding band-edge mode [2]. Despite we can achieve an arbitrarily close spectral gap between the two modes with a sufficiently large  $N$ , the two modes never overlap. Instead, we get densely distributed resonances embedded in the PC band. For this single nanochain, we increase only the pillar number in the longitudinal direction. Increasing the pillar number in the transverse direction by coupling a few single nanochains will be considered in the following sub-section.

Figure 4(c) presents the divergence of the Purcell factor of the four nanochains with the increasing number of particles  $N$ . The sphere nanochain comprises the identical spheres having

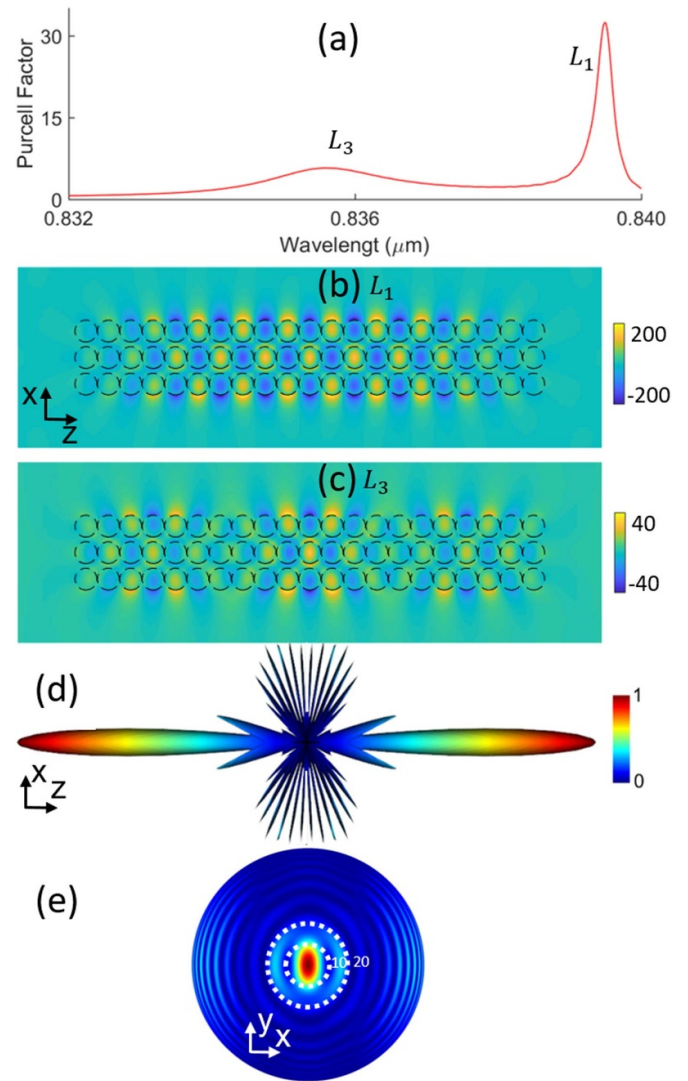
the same parameters as one in figure 2. The pillar nanochain with  $H = 200$  nm has the highest divergence rate but using this height would make other modes appear in the spectral range of interest as one may see from the analysis of figure 1(f). Reducing the height to be  $H = 150$  nm lower the divergence rate, incurred by a higher radiative loss resulting from the smaller transverse aperture of the nanochain. Nevertheless, this pillar nanochain still has a divergence rate higher than that of the sphere nanochain. Further reducing the height  $H$  to 80 nm, we reduce the potential of storing energy in the form of material polarization. Consequently, the radiative loss increases and the divergence rate is the smallest. As a final remark for figures 2(c) and 4(c), we use the suboptimal gap  $G = 10$  nm for those divergence plots to emphasize that the band-edge mode ( $N \rightarrow \infty$ ) results in the infinite Q and Purcell factors even with the sub-optimal gap. In other words, the gap optimization in figure 4(b) is equivalent to the optimization of the band-edge mode of the corresponding PC. This optimization approach is crucial for practically finite structures, especially for collective Mie resonances supported by a few tens of pillars as we will consider next.

### 2.3. Feshbach resonance from coupled pillar nanochains

As discussed in sub-section 2.2.2, we can tune the two  $L_1$  and  $L_3$  modes to be spectrally closer by increasing the pillar number supporting the two collective resonances. Judiciously, we may couple a few nanochains laterally to increase the number of photonic atoms contributing to the collective resonances. Equally important, the inter-chain gap gives us one more tuning parameter.

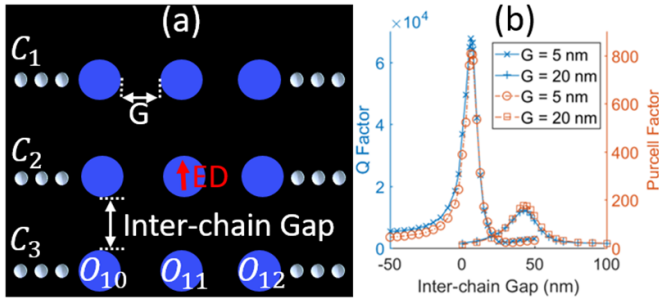
Figure 5 presents the simulation results for three coupled nanochains that support the same collective ED mode presented in figure 3. The coupling of the three coupled nanochains reduces the spectral gap from 20 nm in figure 3(b) to 4 nm in figure 5(a). Figures 5(b) and (c) show the near-field distributions of the two  $L_1$  and  $L_3$  modes of the three coupled nanochains. The near-field strength and hence the Purcell factor associated with the three coupled nanochains is higher than that of the single nanochain in figure 3. These enhancements are due to the reduction of radiative loss to the lateral sides. Figures 5(d) and (e) show the radiation pattern of the  $L_1$  mode. The bidirectional nano-beam has the two main lobes diverging with an estimated solid angle of  $10^\circ$ , fourfold narrower than that presented in figure 3. Furthermore, the side lobes in figure 5(e) are also weaker than those in figure 3(e). The reduction of radiative loss manifests itself in the narrower beam and weaker side lobes. Despite this reduction, the side lobes are still prominent. In other words, the radiative loss is still significant, suggesting that further reduction is possible with optimization. Judiciously, the inter-chain gap in figure 6 plays a similar role as the inter-particle gap  $G$  and indeed we will show that tuning the inter-chain gap will result in the spectral overlap of the two  $L_1$  and  $L_3$  modes.

Figure 6 presents the optimization results for the Q and Purcell factors in two cases with two inter-particle gaps of  $G = 5$  nm and  $G = 20$  nm. Figure 6(a) presents a schematic of the coupled nanochains. Tuning the inter-chain gap leads



**Figure 5.** Collective resonances with the three optically coupled nanochains, each nanochain comprises 21 identical pillars with  $H = 150$  nm,  $D = 230$  nm and  $G = 5$  nm. The inter-chain gap is 50 nm. (a) Spectral plot of the Purcell factor associated with the transverse ED emitter placed at the centre of the photonic molecule. The spectral plot reveals the two resonant modes  $L_1$  and  $L_3$  of which their respective imaginary components of the near-field  $E_x$  distributions are shown in (b) and (c). (d) The radiation pattern corresponding to the  $L_1$  mode shows one bidirectional in-plane beam with many prominent side lobes. (e) The transverse distribution of the radiation pattern.

to the dramatic increases of the Q and Purcell factors of the coupled nanochains for the case of  $G = 5$  nm. These dramatic increases are the signature of a single-mode Feshbach-type BIC nanocavity, also known as supercavity [40]. This Feshbach resonance depends on the two constituent resonances. To understand the effect of these constituent resonances on the overlapping resonance, we compare the results for the two cases of  $G = 5$  nm and  $G = 20$  nm. We choose  $G = 5$  nm and  $G = 20$  nm since they are, respectively, within the optimal range of  $G$  and far from the optimal gap (see figure 4(b)). The case of  $G = 20$  nm corresponds to the constituent resonances having low Q and Purcell factors, i.e. both of the  $L_1$  and  $L_3$



**Figure 6.** Optimization of the Feshbach-type BIC resonance by tuning the inter-chain gap. (a) Schematic of the interaction between the transverse ED emitter and the three nanochains  $C_1$ ,  $C_2$  and  $C_3$ . (b) Cavity performance for the two cases of gap:  $G = 5$  nm and  $G = 20$  nm. The optimal inter-chain gap depends on the periodicity of the single nanochains that are 6 nm and 43 nm for the cases of  $G = 5$  nm and  $G = 20$  nm, respectively.

modes are highly radiative. For the case of  $G = 5$  nm, the dependence on the geometrical parameter is dramatic near the optimal inter-chain gap. The range of the inter-chain gap corresponding to the FWHM of the factors is 10 nm, fivefold smaller than that of the single nanochain in figure 4(a). For the case of  $G = 20$  nm, the Feshbach resonance is weak due to the high radiative loss that manifests itself in the low Q and Purcell factors. The corresponding gap range at FWHM is 25 nm. The shapes of the Q and Purcell factors are similar for both of the cases. This similarity is a characteristic feature of dielectric nanocavities that incur no absorption loss.

Another noteworthy observation from figure 6(b) is about the optimal inter-chain gaps for the two cases that are both larger than the corresponding inter-particle gaps  $G$ . The coupling strength between any two fields trapped by the adjacent photonic atoms are stronger with the smaller gap  $G$ . For our particular case, the optimal inter-chain gaps larger the corresponding inter-particle gaps reflects the fact that the nanocavity has the preferred longitudinal coupling direction. Interestingly, coupling two or more than three nanochains will not result in an overlapping resonance. In other words, the arrangement of the three-coupled nanochains is unique. Judiciously, similar to the single nanochain, for the two coupled nanochains, the number of photonic atoms participating in the collective resonances is not sufficiently large for the two resonances to overlap, even at the optimal inter-chain gap. For more than three coupled nanochains, the structures transform into the regime of two-dimensional cavities with sizes larger than the resonant wavelength. For these two-dimensional structures, the radiative loss to the sides increases. Moreover, other resonant modes will appear as a result of increasing the lateral size and fundamentally we have other cavities with different modes to optimize. Our judicious optimization approach is applicable to two- and three-dimensional structures supporting collective resonances but here we consider the one-dimensional structure for simplicity and clarity of concept discussion. Next we present the nanocavity performance at the optimal inter-chain gap of 6 nm in figure 7.

Reducing the inter-chain gap from 50 nm in figure 5(a) to 6 nm leads to the overlap of the two resonant modes that

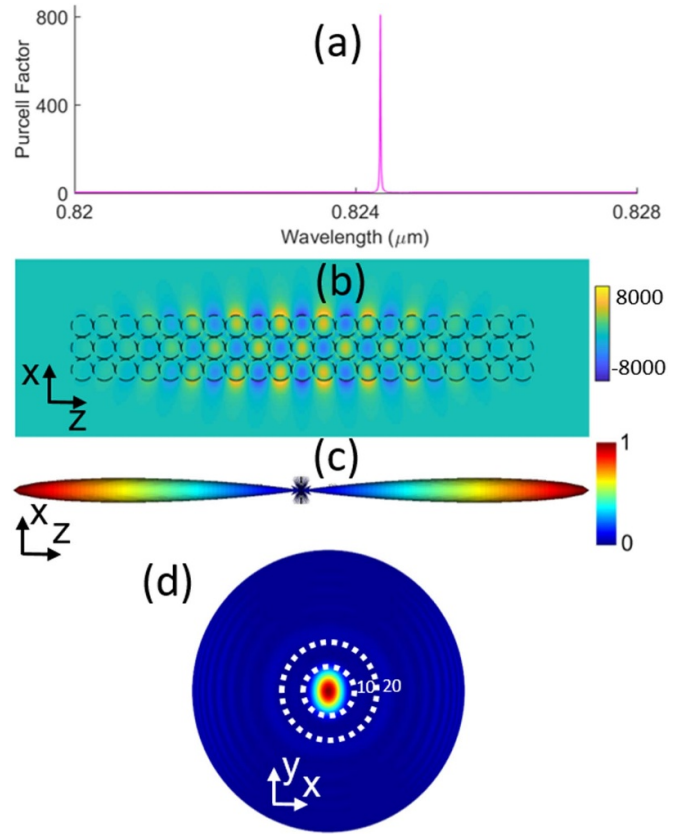


**Figure 7.** High-performance nanocavity with the optimal inter-chain gap of 6 nm. We achieve the single-mode Feshbach-type BIC nanocavity due to the overlap of the two resonant modes  $L_1$  and  $L_3$  that manifests itself in the single peak of the spectral plot in (a). (b) The near-field distribution of the Feshbach-type BIC mode and its corresponding radiation pattern (c). (d) The transverse plot of the radiation pattern shows the in-plane beam diverging into a solid angle of  $10^\circ$  at its full-width at half-maximum intensity.

manifests itself in the single mode in figure 7(a). The optimal Purcell factor increases more than one order of magnitude from 30 in figure 5(a) to 800 in figure 7(a). Associating with this enhancement is the enhancement of the near-field strength as shown in figures 5(b) and 7(b). These enhancements result from the efficient light trapping by the nanocavity by suppressing the radiative loss represented by the side lobes in figure 7(c). A comparison between the transverse plots of the radiation patterns in figures 5(e) and 7(d) corroborates the suppression of the radiative loss. The side lobes in figure 7(d) are negligibly small. Here, it is noteworthy to discuss the far field associated with this Feshbach-type BIC mode. The far-field radiation pattern indicates that the multipole fields are not vanishing. For these radiating multipole fields, their far-field intensities oscillate with amplitudes decreasing as  $r^{-2}$ . More details about the far-field property of these multipole fields can be found in our previous works [21, 23, 24]. Interestingly, this far-field property is also the characteristic feature of general BICs [41].

This single-mode Feshbach-type BIC nanocavity would be useful for applications of nanolaser [2], on-chip quantum light source [42], and on-chip biosensor [43]. Nevertheless, the

stringent requirement of the fabrication accuracy corresponding to the 10 nm FWHM of the gap range would prohibit mass production of the nanocavity for near-IR applications. The fabrication tolerance, which we define as half of the FWHM, may be relaxed greatly for mid-IR wavelength devices since the size sensitivity scales with the wavelength. We will consider a single-mode Feshbach-type BIC nanocavity for mid-IR applications in the following section 3.

### 3. Optimization of L3 PC nanocavity

Silicon photonic integrated circuits operating in mid-IR frequency represent a currently burgeoning field of research with applications, such as free-space communications and lab-on-chip sensors [44, 45]. The remaining critical component for this technology to reach its full potential is mid-IR light source [44, 46]. Narrow-linewidth, chip-scale, single-mode sources with emission wavelengths greater than  $4 \mu\text{m}$  would be ideal for many mid-IR applications but still not yet developed [46]. Recently, a two-dimensional gain material for the mid-IR wavelength range from  $4 \mu\text{m}$  to  $6 \mu\text{m}$  is demonstrated [47]. Owing to the small volume of this two-dimensional material structure, the development of mid-IR laser sources based on such gain materials may require single-mode Feshbach-type BIC nanocavities, such as those presented in section 2. We may choose to scale up the sizes of the photonic pillar atoms for the coupled nanochains to have a resonant wavelength in the mid-IR range and thus pay the way for the application of the single-mode Feshbach-type BIC nanocavity in, for example, mid-IR biosensing [48]. Instead, to emphasize the importance of our judicious design approach based on Feshbach resonance we choose to analyze the well-known L3 PC defect nanocavity [49]. Conceptually important, we will show that the optimal L3 mode indeed corresponds to a Feshbach resonance. We further show the fabrication tolerance for high-performance mid-IR nanocavities to be in the order of 50 nm, which is suitable for mass production using modern fabrication technology.

Figure 8(a) presents a schematic of the L3 PC defect nanocavity. The grey circles with the identical radius  $R$  represent air holes. The three air holes marked by the dash white circles at the centre of the structure have been removed, hence the name of L3. For material, we consider the technologically popular choice of silicon photonic platform. In the mid-IR range, silicon has a refractive index of  $\sim 3.42$ . Additionally, we use a silicon wafer with a sub-wavelength thickness of  $1 \mu\text{m}$  that supports only one mode in the  $y$  direction. With these material and geometrical parameters, we performed a judicious design of the period of the L3 PC nanocavity that results in  $1.3 \mu\text{m}$ . The next step of the optimization process is to study the  $R$  dependence of the Purcell factor associated with a  $z$ -oriented ED emitter placed at the centre of the L3 nanocavity.

Figure 8(b) shows the spectral plots of the Purcell factor with the varying radius in a step size of  $100/3 \text{ nm}$ . We observe the highest Purcell factor with  $R$  in the range from 300 nm to 333 nm. More importantly, we observe the two distinct modes:  $M_1$  and  $M_2$ . Figure 8(b) also indicates that the  $R$  range

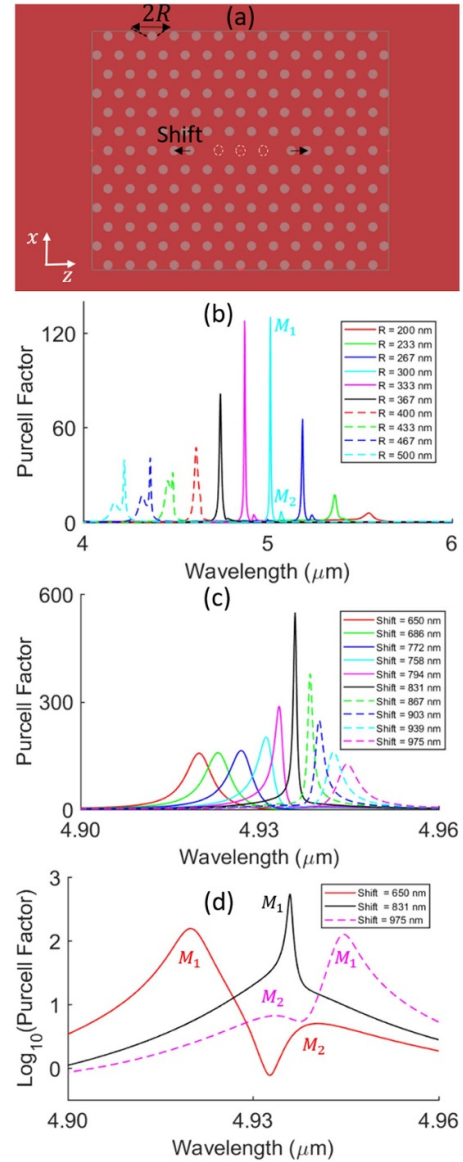


**Figure 8.** Optimization of the L3 PC defect nanocavity for applications in mid-IR silicon photonics. The silicon wafer has a thickness of  $1 \mu\text{m}$  and the PC period is designed to be  $1.3 \mu\text{m}$ . (a) Schematic of the L3 PC cavity. (b) Varying the radius  $R$  of the air holes results in the cavity having two modes of  $M_1$  and  $M_2$  at  $R = 300 \text{ nm}$ . (c) Varying the Shift distance for the case of  $R = 333 \text{ nm}$  in (b) results in the dramatic enhancement of the Purcell factor when the hole shift equals to  $831 \text{ nm}$ . (d) The three plots in (c) are re-plotted in logarithmic scale to illustrate the crossing of the two modes  $M_1$  and  $M_2$  at the Shift of  $831 \text{ nm}$ .

corresponding to the FWHM of the Purcell factor is  $\sim 100 \text{ nm}$  ( $\Delta R \sim 367 - 267 = 100 \text{ nm}$ ). The two  $M_1$  and  $M_2$  modes are spectrally close and judiciously inspire us to optimize the nanocavity in the framework of Feshbach resonance by looking for geometrical parameters for tuning the two modes. The radius  $R$  is one possible tuning parameter. Indeed, we achieve the overlap with the radius  $R = 400 \text{ nm}$ . Nevertheless, unlike the Feshbach's overlapping resonance of the  $L_1$  and  $L_3$  modes with  $G = 5 \text{ nm}$  in sub-section 2.3, the overlapping resonance from these  $M_1$  and  $M_2$  modes does not correspond to a

dramatic increase of the Purcell factor. The reason is that by increasing the radius of the air holes, we reduce the silicon volume for storing energy in the form of material polarization. In turn, this reduction will destroy the optimal balance between the electric and magnetic energies stored in the cavity structure. In this step of  $R$  optimization, we achieve the optimal balance around  $R = 333$  nm. Destroying the optimal balance will increase the radiative losses for both the  $M_1$  and  $M_2$  modes [50]. Consequently, the overlapping mode of the  $M_1$  and  $M_2$  modes also has a high radiative loss, i.e. the overlapping resonance is spectrally broad as observed from the plot for  $R = 400$  nm.

The above analysis would motivate one to find an alternative geometrical parameter for tuning the interfering resonance between the two  $M_1$  and  $M_2$  modes. In the next step of optimization, we fix the radius at  $R = 333$  nm and shift the two air holes at the two ends by a distance as shown schematically in figure 8(a). In fact, the discovery of the high-performance L3 PC defect cavity originated from the analysis of minimizing the radiative loss by shifting the air holes [45]. Here, we show that similar to the interfering resonance between the two  $L_1$  and  $L_3$  modes presented in section 2.3, the physical mechanism responsible for the reduction of the radiative loss is the destructive interference of the scattering field in the directions of side lobes. Figure 8(c) shows the plots of the Purcell factor with the varying Shift distance. At the optimal Shift of 831 nm, we observe a single-mode Feshbach-type BIC resonance that manifests itself in the dramatic increase of the Purcell factor. This dramatic increase is equivalent to a near-field enhancement according to equation (4), which is physically due to the efficient trap of emission light by means of destructive interference of the scattering field. One may estimate the FWHM range of the Shift from figure 8(c) to be  $\sim 100$  nm ( $903 - 794 = 109$  nm). To see the clear evidence of the overlap between the two modes at the shift of 831 nm, we replot the Purcell factor for the three shift distances of 650 nm, 831 nm, and 975 nm in the logarithmic scale in figure 8(d). The spectral distance between the two  $M_1$  and  $M_2$  modes for the 650 nm Shift is 20 nm, reducing from 50 nm for the two modes without shift as presented in figure 8(b). Increasing the Shift distance to 831 nm makes the  $M_2$  mode to disappear and the  $M_1$  mode resonates strongly. Increasing the Shift distance further to 975 nm, we observe the relative crossing of the  $M_2$  mode from the left to the right side of the  $M_1$  mode. This spectral crossing is clear evidence of Feshbach resonance.

This section has emphasized again that one must fulfill the two requirements for a successful design of the Feshbach-type (quasi-)BIC nanocavity. First, we must have the spectral overlap of the interfering cavity modes by tuning geometrical parameters. Second, the tuning must ensure that the cavity structure always supports at least one constituent mode having a high Q factor.

#### 4. Conclusion

This work presents the analytical modelling of collective Mie resonances based on the exact solutions to the Maxwell

equations. Based on this theory, we develop the judicious design approach of single-mode Feshbach-type BIC nanocavities. We provide the two design showcases of the high-performance nanocavities. First, we optimize the unique structure of the three coupled nanochains for near-IR frequency applications. With the optimal geometrical parameters, the high-performance nanocavity suppresses strongly the side lobes of the bidirectional beam. These side lobes represent the radiative loss channels of the nanocavity mode. In the second showcase, we analyze and optimize the well-known L3 PC defect nanocavity for mid-IR applications based on Feshbach's unified theory of resonance. We show the suppression of the radiative loss associated with the original design of the L3 PC nanocavity that is due to the overlap of the two resonant modes.

Conceptually, we discuss and distinguish Mie resonant modes (whispering-gallery modes of a spherical cavity), collective Mie resonant modes, PC cavity modes, and Feshbach-type BIC modes (supercavity modes). Since the Maxwell equations can be reformulated into the Schrödinger form that indicates the light energy is always higher than its potential in all-dielectric systems, all electromagnetic modes in an infinite all-dielectric system with infinite Q factors are technically BICs. In this definition, many band-edge PC modes, such as those resulting from collective Mie resonances, are BICs. For practically finite structures, all BIC modes manifest themselves in resonant modes with finite Q factors. For these resonant modes, optimization of geometry is crucial, as we demonstrate with the collective Mie resonances in this work. The rich physics of collective Mie resonances offered by the freedom of arranging photonic atoms to form photonic molecules may open up possibilities for controlling light-matter interaction efficiently enough for both near- and mid-IR frequency applications.

#### Data availability statement

All data that support the findings of this study are included within the article.

#### Acknowledgment

This research is supported by A\*STAR under its Career Development Fund (C210112012).

#### ORCID iD

Thanh Xuan Hoang  <https://orcid.org/0000-0002-6815-487X>

#### References

- [1] Ma R-M and Oulton R F 2019 *Nat. Nanotechnol.* **14** 12
- [2] Hoang T X, Ha S T, Pan Z, Phua W K, Paniagua-Domínguez R, Png C E, Chu H-S and Kuznetsov A I 2020 *Nano Lett.* **20** 5655

- [3] Lodahl P, Mahmoodian S and Stobbe S 2015 *Rev. Mod. Phys.* **87** 247
- [4] Reiserer A and Rempe G 2015 *Rev. Mod. Phys.* **87** 1379
- [5] Bayer M, Gutbrod T, Reithmaier J P, Forchel A, Reinecke T L, Knipp P A, Dremin A A and Kulakovskii V D 1998 *Phys. Rev. Lett.* **81** 2582
- [6] Kuznetsov A I, Miroshnichenko A E, Brongersma M L, Kivshar Y S and Luk'yanchuk B 2016 *Science* **354** aag2472
- [7] Decker M, Staude I, Falkner M, Dominguez J, Neshev D N, Brener I, Pertsch T and Kivshar Y S 2015 *Adv. Opt. Mater.* **3** 813
- [8] Hoang T X, Nagelberg S N, Kolle M and Barbastathis G 2017 *Opt. Express* **25** 13125
- [9] Liao K, Hu X, Gan T, Liu Q, Wu Z, Fan C, Feng X, Lu C, Liu Y-C and Gong Q 2020 *Adv. Opt. Photonics* **12** 60
- [10] Kruk S and Kivshar Y 2017 *ACS Photonics* **4** 2638
- [11] Hsu C W, Zhen B, Stone A D, Joannopoulos J D and Soljacic M 2016 *Nat. Rev. Mater.* **1** 16048
- [12] Feshbach H 1958 *Ann. Phys., NY* **5** 357
- [13] Friedrich H and Wintgen D 1985 *Phys. Rev. A* **32** 3231
- [14] Fano U 1961 *Phys. Rev.* **124** 1866
- [15] Fano U 1935 *Nuovo Cimento D* **12** 156
- [16] Chin C, Grimm R, Julienne P and Tiesinga E 2010 *Rev. Mod. Phys.* **82** 1225
- [17] Schulz G J 1973 *Rev. Mod. Phys.* **45** 378
- [18] Hoang T X, Chen X and Sheppard J R C 2012 *Phys. Rev. A* **86** 033817
- [19] Gouesbet G 2019 *J. Quant. Spectrosc. Radiat. Transfer* **230** 247
- [20] Devaney A J and Wolf E 1974 *J. Math. Phys.* **15** 234
- [21] Hoang T X, Chen X and Sheppard J R C 2014 *Opt. Express* **22** 8949
- [22] Hoang T X, Duan Y, Chen X and Barbastathis G 2015 *Opt. Express* **23** 12337
- [23] Hoang T X, Chen X and Sheppard J R C 2012 *J. Opt. Soc. Am. A* **29** 32
- [24] Hoang T X, Chen X and Sheppard J R C 2013 *J. Opt. Soc. Am. A* **30** 1426
- [25] Mishchenko M I, Zakharova N T, Khlebtsov N G, Videen G and Wriedt T 2017 *J. Quant. Spectrosc. Radiat. Transfer* **202** 240
- [26] Glauber R J and Lewenstein M 1991 *Phys. Rev. A* **43** 467
- [27] Ho T D, Knoll L and Welsch D-G 1998 *Phys. Rev. A* **57** 3931
- [28] Xu Y, Lee R K and Yariv A 2000 *Phys. Rev. A* **61** 033807
- [29] Novotny L and Hecht B 2012 *Principles of Nano-Optics* (Cambridge: Cambridge University Press)
- [30] Purcell E M 1946 *Phys. Rev.* **69** 681
- [31] Miroshnichenko A E, Evlyukhin A B, Yu Y F, Bakker R M, Chipouline A, Kuznetsov A I, Luk'yanchuk B, Chichkov B N and Kivshar Y S 2015 *Nat. Commun.* **6** 8069
- [32] Wei L, Xi Z, Bhattacharya N and Urbach H P 2016 *Optica* **3** 799
- [33] Devaney A J and Wolf E 1973 *Phys. Rev. D* **8** 1044
- [34] Lagendijk A and van Tiggelen B A 1996 *Phys. Rep.* **270** 143
- [35] (Available at: [www.lumerical.com/products/fdtd/](http://www.lumerical.com/products/fdtd/))
- [36] Stillinger F H 1976 *Physica B* **85** 270
- [37] Yablonovitch E 2007 *Opt. Photonics News* **18** 12
- [38] Kodigala A, Lepetit T, Gu Q, Bahari B, Fainman Y and Kanté B 2017 *Nature* **541** 196
- [39] Ha S T, Fu Y H, Emani N K, Pan Z, Bakker R M, Paniagua-Domínguez R and Kuznetsov A I 2018 *Nat. Nanotechnol.* **13** 1042
- [40] Rybin M and Kivshar Y 2017 *Nature* **541** 164
- [41] Fonda L 1963 *Ann. Phys., NY* **22** 123
- [42] Liu F et al 2018 *Nat. Nanotechnol.* **13** 835
- [43] Yavas O, Svedendahl M, Dobosz P, Sanz V and Quidant R 2017 *Nano Lett.* **17** 4421
- [44] Hu T, Dong B, Luo X, Liow T-Y, Song J, Lee C and Lo G-Q 2017 *Photon. Res.* **5** 417
- [45] Lin H, Luo Z, Gu T, Kimerling L C, Wada K, Agarwal A and Hu J 2018 *Nanophotonics* **7** 393
- [46] Shim E, Gil-Molina A, Westreich O, Dikmelik Y, Lascola K, Gaeta A L and Lipson M 2021 *Commun. Phys.* **4** 268
- [47] Lukman S et al 2020 *Nat. Nanotechnol.* **15** 675
- [48] Leitis A, Tseng M L, John-Herpin A, Kivshar Y S and Altug H 2021 *Adv. Mater.* **33** 2102232
- [49] Akahane Y, Asano T, Song B-S and Noda S 2003 *Nature* **425** 944
- [50] Khurgin J B and Sun G 2014 *Nat. Photon.* **8** 468